Engineering Fracture Mechanics 333 (2026) 111833

Contents lists available at ScienceDirect

Engineering Fracture Mechanics

journal homepage: www.elsevier.com/locate/engfracmech

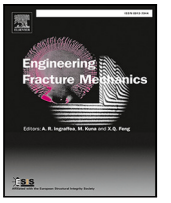

Fracture Mechanics in Smoothed Particle Hydrodynamics: An algorithm to calculate the J-Integral

Tom De Vuyst [a,*], Rade Vignjevic [b], Nenad Djordjevic [b,c], Marius Gintalas [d], Kevin Hughes [b,e]

[a] University of Hertfordshire, Centre for Engineering Research, Materials and Structures Group, College Lane, Hatfield, AL10 9AB, Hertfordshire, UK
[b] Brunel University of London, Centre for Assessment of Structures and Materials under Extreme Conditions, Department of Mechanical and Aerospace Engineering, Kingston Lane, Uxbridge, UB8 3PH, UK
[c] Institute for Information Technology Kragujevac, Jovana Cvijica bb, Kragujevac, 34000, Serbia
[d] Klaipėda University, Marine Research Institute, Mechanical and Marine Engineering Laboratory, 17 Universiteto avenue, Klaipėda, LT-92294, Lithuania
[e] University of Derby, College of Science and Engineering, Markeaton Street, Derby, DE22 3AW, UK

ARTICLE INFO

Keywords:
J-integral
Linear Elastic Fracture Mechanics (LEFM)
Smoothed Particle Hydrodynamics (SPH)
Single Edged Notch Tension (SENT)
Finite Element Method (FEM)
Fracture

ABSTRACT

The stress intensity factors or strain energy release rate are typically used to characterise the stress field in the vicinity of a crack in fracture mechanics. One way to obtain the strain energy release rate in elastic–plastic fracture mechanics is from the stress and deformation field around the crack tip through the calculation of the J integral. The J-integral is contour independent, although the contour must start and end from a traction-free surface, such as the crack surface. Using Green's theorem, the J-integral can be formulated as a surface or area integral, which makes it convenient for implementation in finite element method (FEM). More importantly, the J-integral calculation is insensitive to uncertainty of the exact crack tip location, can be applied for linear elastic analysis with small scale yielding and in an improved formulation for elastic–plastic fracture. In short, the J-integral is an indispensable tool in the study of fracture mechanics.

Despite the J-integral being widely used in FEM, including availability in most commercial FEM codes, there is currently no algorithm to calculate the J-integral in the Smoothed Particle Hydrodynamics (SPH) method. This is somewhat surprising since the SPH method, due to its meshless nature, has inherent advantages in dealing with cracks compared to mesh based methods such as FEM. In this paper we will therefore address this deficiency and develop an algorithm for calculation of the J integral in the SPH method. The implementation of his new alghorithm is based on a new definition of the weighting function q_1, as appropriately normalised kernel function, which inherently satisfies all the specific requirements on q_1: The function is sufficiently smooth in the J-integral area, it is equal to unit inside contour path of the integral and zero outside of the path. A further element of novelty is that in the current implementation, the gradient of this function is evaluated analytically rather than through a numerical approximation. The verification and validation of developed algorithm is based on simulation of the standard single edge notch tension test (SENT) under the plain strain conditions. The SPH results are compared to the FEM results for stress and displacement fields in the vicinity of the crack tip, as well as the J integral solutions. The SPH results demonstrated convergence and were within 2% of the converged FEM solutions.

* Corresponding author.
E-mail address: t.de-vuyst@herts.ac.uk (T. De Vuyst).

https://doi.org/10.1016/j.engfracmech.2025.111833
Received 23 August 2025; Received in revised form 23 December 2025; Accepted 30 December 2025
Available online 31 December 2025

The validation also allows for the definition of simple guidelines for the definition of the J-integral area to achieve accurate results. The implementation is currently developed for linear elastic fracture mechanics applications, but its generalisation and application to elastic–plastic fracture mechanics, including the combination with elastic–plastic constitutive models is straightforward.

1. Introduction

Fracture mechanics allows for the identification and quantification of the conditions necessary for unstable crack propagation, i.e. catastrophic failure, in many structures. Generally, this requires knowledge of both the material's fracture characteristics, e.g. toughness and the energy release rate for the defect in question. Numerical methods, such as the Finite Element Method (FEM) but also meshless methods such as Smoothed Particle Hydrodynamics (SPH) [1–5], enable the determination of the stress and deformation fields in almost any structural component under a wide range of loading conditions. The energy release rate for particular defects can be calculated from the numerically determined equilibrium fields. For isotropic linear elastic solids, the dominant asymptotic stress, strain, and displacements fields in vicinity of the crack tip scale linearly with the stress intensity factor (SIF) K, as defined in [6]. K is related to the energy release rate G and the J integral [7] having in mind the one to one correspondence, $G = J$ [8]. Consequently, SIF and strain energy release rates are the key parameters for the assessment of structural integrity using the linear elastic fracture mechanics. Thus, it is the quantities, K and J, which we seek to extract from numerical solutions.

In materials exhibiting elasto-plastic deformation, the near-tip (plastic) asymptotic behaviour, under certain restricted conditions, is represented by a family of self-similar fields. For materials which obey power-law or linear strain-hardening constitutive relationships and experience nearly proportional loadings, these fields are known as the HRR fields [8,9] and have the distinctive characteristic of scaling with J in a way dependent on the strain hardening exponent. Another area where the J-integral is commonly used is in the modelling of delaminations in multi-layer composite structures [10,11].

The stress intensity factor, K, and the J integral are used for defect assessment in a number of structural engineering standards such as BS7910 [12]. In these assessments numerical modelling is routinely used for evaluation of the J-integral values at a flaw. Several procedures have been developed to extract K and J from FE solutions, and these are available in many commercial FEM codes [13,14]. Although at this stage we only consider standard FEM and SPH techniques it is worth specifically highlighting the virtual crack closure technique (VCCT) to calculate energy release rate in FEM [15,16] and the Extended Finite Element Method (XFEM) [17,18] as important numerical techniques used in fracture mechanics to accurately model crack propagation without requiring mesh refinement. Unlike traditional FEM, XFEM enriches the solution space by incorporating special functions that capture singularities and discontinuities within standard finite element meshes. In J-integral calculations, XFEM plays a crucial role by allowing discontinuities to be represented within standard finite element meshes. This eliminates the need for complex remeshing as cracks grow, making simulations more efficient and accurate. In addition, XFEM allows for more accurate representation of the singular stress field near the crack tip and consequently enhances the accuracy of J-integral evaluations. This method is particularly useful in analysing fatigue crack growth, stress intensity factors, and fracture toughness in structures subjected to variable loads and with complex geometries. However, the method faces challenges in maintaining accuracy when dealing with complex geometries [19].

For instance, in three-dimensional cracked bodies, even under uniform loading, the magnitude of stress and deformation varies through the thickness of the specimen along the crack front. Studies with standard compact test (CT) specimens have shown that the SIF, i.e. J-integral tends to be highest at the midplane and lowest at the free surface [20]. This variation is due to differences in constraint conditions: the midplane experiences higher constraint, leading to greater energy release rates, while the free surface has lower constraint, reducing the J-integral value. The ability to accurately assess and predict these effects is fundamental to structural safety.

The SPH meshless method is inherently well suited for modelling damage, fracture and failure of solids and structures under monotonic and/or dynamic loading. Typical applications are modelling of ballistic impact and fragmentation modelling [21–24], and these illustrate, due to its meshless nature, the strength of SPH in the ease with which failure (necking, shear bands, ...) and cracks can be modelled. More recently some researchers have started to investigate the use of the SPH for fatigue and fracture mechanics problems [25–28]. They highlight the ease with which the geometry can be discretised around the crack tip as another advantage of the SPH method for this type of problems, and develop crack propagation algorithms based on the stress intensity factor and Paris' Law. The focus in their work lies on the representation of the crack growth, i.e. the progression of the crack front and the representation of the discontinuity in the displacement and stress fields at the crack surface. They rely on resolving the stress field in the vicinity of the crack tip and correlating this with the theoretical stress distribution to estimate the Stress Intensity Factor, K. From this survey of the current state-of-the-art on to analysis of fatigue and fracture mechanics problems with the SPH method, it is clear that there is a limited amount of work on this topic. Specifically, the absence of a method to calculate the J-integral in the SPH method can be considered a major obstacle in the use of the SPH method for fracture mechanics problems.

A specific engineering example where SPH based fracture modelling have demonstrated potential is problems involving fluid–solid interaction phenomena. For instance, coupled liquid flow and solid deformation in porous materials has a wide range of applications, such as wave-porous structure interaction in coastal, hydraulic fracturing in geotechnical or carbon dioxide capturing in

Nomenclature

$\mathbf{a}$	Acceleration vector
$\mathbf{E}$	Green–Lagrange strain tensor
$\mathbf{F}$	Deformation gradient tensor
G	Strain energy release rate
$\mathbf{I}$	Second order identity tensor
J	Value of the J-integral
Jac	Jacobian
K	Stress intensity factor
n_i, n_1	Normal vector, component of n in direction of the crack
$\mathbf{P}$	Nominal stress tensor
q	J-integral weighting function
$\mathbf{u}$, u_i	Displacement vector
U	Internal Energy
V, V^0	Particle volume, particle initial volume
W	Kernel function
δ_{ij}	Kronecker delta function
ε	Strain rate tensor
ρ, ρ_0	Density, initial density
σ, σ_{ij}	Cauchy stress tensor

environmental engineering [29]. Conventional FEM is commonly used to solve the coupled flow-deformation problem including the application of J-integral as fracture parameter [30,31]. However, these methods often cannot efficiently handle large deformations in post-failure stage [29]. SPH offers an advantages in this domain as it deals better with large deformations and eliminates mesh distortion issue [31,32]. Thus having J-integral computation algorithm implemented in SPH, would allow to simulate and quantify fracture as it is done in FEM, but without the mentioned drawbacks.

The purpose of the current paper is therefore to address this issue and develop an SPH algorithm for the calculation of the J-integral, and to assess its capabilities relative to FEM models. The paper is structured as follows: following this introduction, Section 2 summarises the specific SPH scheme used in the simulations and Section 3 then discusses on the development of the algorithm to calculate the J-Integral in SPH, this is then followed by a section with the description of the validation test and the reference FEM solutions. The Section 5 contains the SPH model results, including a study of different modelling choices. The paper is completed with the outline on the findings in the conclusion section.

2. Summary of total Lagrange SPH algorithm used

The explicit Total-Lagrangian form of SPH was used for this investigation with a central difference time integration scheme. The use of a Total-Lagrangian form ensures stability in tension. The Total Lagrange SPH formulation evaluates all kernel sums in the reference configuration (indicated by the use of sub/superscripts 0 in the following equations). A detailed description of the algorithm used can be found in [33], but the main equations for each time step are as follows: The deformation gradient $\mathbf{F}$ is calculated using:

$$\langle \mathbf{F} \rangle_i = -\sum_j V_j^0 \left(\mathbf{u}_j - \mathbf{u}_i\right) \otimes \nabla_0 W_{ij} + \mathbf{I} \tag{1}$$

From which the rate-of-deformation $\dot{\boldsymbol{\varepsilon}}$ can be calculated via push-forward of the Green–Lagrange strain rate $\dot{\mathbf{E}}$ to the current configuration:

$$\dot{\mathbf{E}} = \frac{1}{2}\left[\dot{\mathbf{F}}^T\mathbf{F} + \mathbf{F}^T\dot{\mathbf{F}}\right] \tag{2}$$

$$\dot{\boldsymbol{\varepsilon}} = \mathbf{F}^{-T}\dot{\mathbf{E}}\mathbf{F}^{-1} \tag{3}$$

From this the increment in Cauchy stress $\boldsymbol{\sigma}$ is calculated and pulled back into the Nominal Stress $\mathbf{P}$:

$$\mathbf{P} = \mathrm{Jac}\,\mathbf{F}^{-1}\boldsymbol{\sigma} \tag{4}$$

The momentum equation is then solved to obtain the new accelerations $\mathbf{a}$:

$$\langle \mathbf{a} \rangle_i = -\sum_j V_j^0 \left(\frac{\mathbf{P}_j}{\rho_{0,j}^2} + \frac{\mathbf{P}_i}{\rho_{0,i}^2}\right) \cdot \nabla_0 W_{ij} \tag{5}$$

From the particle accelerations the new velocities and positions are calculated using the central difference equations to complete the time step. Unless stated otherwise, a cubic B-spline kernel function is used to evaluate Eqs. (1) and (5).

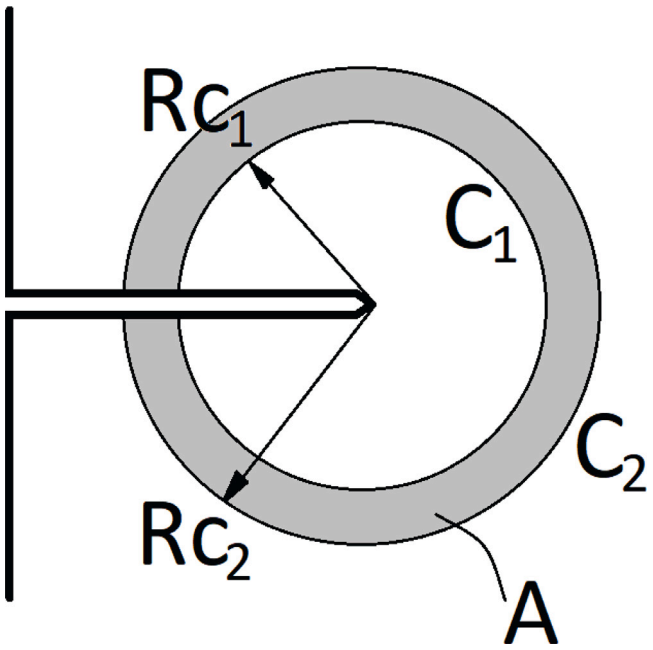

Fig. 1. Diagram showing definition of J-Integral.

3. Development of SPH J-integral expression

3.1. J-Integral as a surface integral in 2D

In the case of a non-linear elastic solid and assuming two-dimensional plane strain, Rice [8] showed that the J-Integral, evaluated on a closed contour about the crack tip, is path independent in conservative material systems in the absence of crack-face tractions, body forces, and thermal strains [8]. Following the work by Shih and co-authors [34–37] the J-Integral for general static conditions can be expressed in a Cartesian coordinate system [34] as:

$$J = \int_{\Gamma} \left[U n_1 - \sigma_{ij} n_i \frac{\partial u_j}{\partial x_1} \right] \mathrm{d}s \tag{6}$$

Here the x_1 axis is parallel with the crack direction, Γ is any contour beginning at the bottom crack face and ending on the top crack face, n_i is the unit vector outward normal of contour Γ, U is the strain–energy density, σ_{ij} is Cauchy stress and u_i is the displacement vector. Further, following Shih et al. [34] this surface integral can be written as a volume integral through the introduction of weighting function q_1. The requirement for function q_1 is that it is a sufficiently smooth function in the area A, and that it is unity on the inside path, C_1, and zero on and outside the path, C_2, see Fig. 1.

The general expression for the J Integral in two-dimensions, applicable to cracks with no crack face traction, no body force and no thermal stresses, can be written as a volume integral as [34]:

$$J = \int_{A} \left[\sigma_{ij} \frac{\partial u_i}{\partial x_1} - U \delta_{1j} \right] \frac{\partial q_1}{\partial x_j} \mathrm{d}A \tag{7}$$

where q_1 is a sufficiently smooth function in A that is unity, $q_1 = 1$, on C_1 and vanishes, $q_1 = 0$ on C_2. In the numerical evaluation of Eq. (7) C_1 is typically shrank to a point at the crack tip. In Finite Element Method (FEM) based calculations of the J-Integral the q_1 function is generally defined as a piecewise continuous function defined by nodal values. This means that the function q_1 has to conform to the mesh and the value of q_1 has to be 0 on the outer contour and 1 on the inner contour. When evaluating the integral in Eq. (7) using FEM, the values of the gradient of q_1 are required at the integration points and are obtained using the element shape functions, usually Lagrange polynomials. In contrast the use of meshless methods such as SPH offers some interesting alternatives to this which will be described below and evaluated in the results section. Firstly, we observe that the choice of the q_1 function in the SPH method offers much more freedom. The q_1 function does not need to conform to any mesh and can for example be defined as an appropriately re-normalised kernel function ($q_1 = 1$ at centre and 0 on the external boundary). The advantage of this approach is that there are no special requirements in terms of discretisation. The crack and contour boundary of the area in the J-Integral formulation does not have to be located on particles, i.e. there are no specific requirements on the particle distribution around the crack tip (other than it is sufficient to accurately capture displacement and stress fields). Consequently the J-Integral area in this paper (2D problem) is simply defined as a circle. A second advantage, resulting from the choice of q_1 as a SPH kernel-type function, is that the gradient can simply be calculated analytically at each particle (integration point). So it is sufficient that q_1 is

differentiable, and simplifies the calculation of the J-integral and avoids inaccuracies that could be introduced when approximating the gradient of q_1 numerically as is the case in FEM.

3.2. Implementation of J-Integral in SPH as a surface integral in 2D

For the implementation of the integral in Eq. (7) in the SPH method we consider the Total Lagrangian SPH framework [33]. Initial results (Sections 6 and 7) in this paper are obtained using a cubic B-spline kernel function:

$$\begin{aligned} W &= C\left(\frac{3}{4}z^3 - \frac{3}{2}z^2 + 1\right) && z < 1 \\ W &= \frac{C}{4}(2-z)^3 && 1 \le z < 2 \\ W &= 0 && z \ge 2 \end{aligned}$$

$$\begin{aligned} \nabla W &= C\left(\frac{9}{4}z^2 - 3z\right)\frac{\mathbf{x}_i - \mathbf{x}_j}{zh^2} && z < 1 \\ \nabla W &= -\frac{3C}{4}(2-z)^2\frac{\mathbf{x}_i - \mathbf{x}_j}{zh^2} && 1 \le z < 2 \\ \nabla W &= 0 && \ge 2 \end{aligned}$$

where $z = \left|\mathbf{x}_i - \mathbf{x}_j\right|/h$, and C is a normalisation constant. In Section 8 the effect of using different q_1 functions will be studied.

The integral is evaluated point-wise over the set of particles inside the integral's domain, i.e. the volume integral is replaced by a sum over all particles that lie inside the volume, and Eq. (7) becomes:

$$J = \sum_{a \in A} V_a \left[\sigma_{ij}\frac{\partial u_i}{\partial x_1} - U\delta_{1j}\right]_a \left\langle \frac{\partial q_1}{\partial x_j}\right\rangle_a \tag{8}$$

This integral is written in the current (deformed) configuration and is a sum of all particles a that lie within the area A. In this configuration the state variables are the current density, ρ_a and the stress is the Cauchy stress, σ and strain energy density U, the last two are already calculated during the stress update in the constitutive model. The particle volume is V_a. Finally, the displacement gradient tensor in the current configuration, $\partial u_j/\partial x_i$, is easily obtained. When using the Total Lagrange formulation the deformation gradient F is calculated, and the displacement gradient in the current configuration can be calculated using:

$$\frac{\partial u_\alpha}{\partial x_\beta} = \delta_{\alpha\beta} - F^{-1}_{\alpha\beta} \tag{9}$$

As mentioned earlier, the gradient of function $q_1\left(x_a\right)$, for particle a, in Eq. (8) is the analytically calculated derivative of the cubic B-spline kernel $W\left(\mathbf{x}_i, \mathbf{x}_j, h\right)$ with kernel support radius C_2, i.e. $2h = R_{C_2}$ and normalisation constant such that at the centre of the circle, x_c located at the crack tip, $W\left(\mathbf{x}_c, \mathbf{x}_c, h\right) = 1$, see Fig. 2. The expression for the gradient of q_1 then becomes:

$$\begin{aligned} \nabla q_1 &= \frac{1}{W\left(\mathbf{x}_c, \mathbf{x}_c, h\right)} C\left(\frac{9}{4}z^2 - 3z\right)\frac{\mathbf{x}_i - \mathbf{x}_j}{zh^2} && z < 1 \\ \nabla q_1 &= -\frac{1}{W\left(\mathbf{x}_c, \mathbf{x}_c, h\right)}\frac{3C}{4}(2-z)^2\frac{\mathbf{x}_i - \mathbf{x}_j}{zh^2} && 1 \le z < 2 \\ \nabla q_1 &= 0 && \ge 2 \end{aligned} \tag{10}$$

The proposed algorithm is presented as a block diagram in Fig. 3. In terms of computational efficiency, the calculation of the J-integral is done as a post-processing operation (i.e. after the stress and displacement field has been calculated), similar to FEM. It is not a computationally expensive operation which can be understood by considering the example of the largest model used in this paper, and which has 140000 particles in total. Every particle has around 20 neighbours, so a total of 2800000 particle interactions need to be evaluated for each time step. In contrast the largest J-integral calculation has around 3000 particles with a similar calculation effort per particle, so the computational effort for the calculation of the J-integral is around 3 orders of magnitude lower than the effort to solve for the stress and displacements.

4. Test problem finite element model and reference data

The SPH form of the two dimensional J-integral is investigated through comparison of SPH results with a FEM reference solution. FE solution was validated against solution available from [38]. The test problem used in this paper is a 2D plane strain model of a Single Edge Notch Tension (SENT) specimen, shown in Fig. 4. The specimen has a total length of 50 mm and width 10 mm with a single crack located at the mid-point. The crack-length is equal to half the specimen width. The ends are clamped and a total extension in the axial (along the X-direction of 0.0507664 mm is applied to the specimen. In all models this is applied as a prescribed displacement in the axial direction of the specimen of 0.0253882 mm at each end. The purpose of selecting a clamped boundary condition is represent the actual test conditions and to define a set of boundary conditions that can be consistently applied in the different numerical methods and models. The material is elastic, with elastic modulus equal to 210 GPa, Poisson's ratio is 0.3 and density is 7800 kg/m^3.

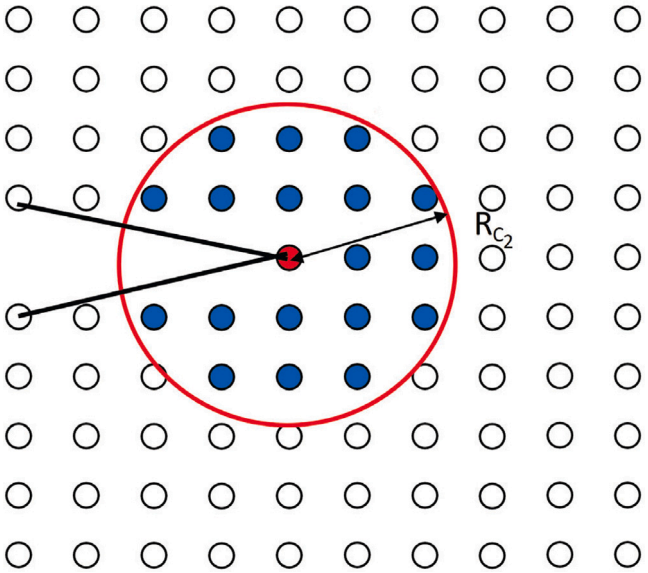

Fig. 2. Definition of J-Integral area on SPH discretisation.

Table 1
FEM Models developed with Plain Strain 2D quadratic elements with and without focused mesh around the crack tip.

FEM model	Number of elements			
	Width	Length	Along crack face	Total
Focussed 20 (F20)	20	100	10	2380
Focussed 40 (F40)	40	200	20	9403
Focussed 80 (F80)	80	400	40	37 639
Focussed 160 (F160)	160	800	80	152 210
Not focussed 20 (NF20)	20	100	10	2000
Not focussed 40 (NF40)	40	200	20	8000
Not focussed 80 (NF80)	80	400	40	32 000
Not focussed 160 (NF160)	160	800	80	128 000

4.1. Reference finite element models

Finite element models are developed using the ABAQUS CAE 2023 FE software [13] to provide reference solutions for comparison with the SPH model results. The models are developed by using standard 8-node biquadratic plane strain quadrilateral elements, CPE8, with aspect ratio 1 and the mesh density equivalent to the discretisation density in SPH models. Two modelling approached were developed, with and without focused mesh at the crack tip to analyse the sensitivity of the results and to match the approach used with SPH. Two models with the coarsest mesh, with 20 elements along the width, are shown in Fig. 5, whilst the mesh density for the other developed models are given in Table 1. J-Integral values were evaluated using the *CONTOUR INTEGRAL function, available in Abaqus, where the geometry of the crack is defined in terms of the node representing the crack tip and a vector in direction of the crack propagation. The model was developed to represent the $1/\sqrt{r}$ type of singularity in strain at the crack tip, with the mid side node of the wedge elements being 0.25 times the edge length away from the crack tip. This setup improves the accuracy of the results for J integral. The J integral is evaluated for a number of contours specified as input. The contours are defined in terms of rings of elements surrounding the crack tip [13,39], starting from the first contour consisting of elements connected to the crack tip node. The subsequent contours are defined by adding a ring of elements that share nodes with the previous contour to the domain defined as the previous contour, as illustrated in Figs. 6 and 7. The weighting function q_1 is zero at the nodes outside of the contour and one inside the contours at element corner nodes. The function takes a value between zero and one at the mid-side nodes according to the position of the node on the side of the element.

The full FEM results for the J-integral are listed in Table 4, but essentially from the third contour onwards the J-integral values converge to a value of 6786 J/m^2 and 6785 J/m^2 for the focussed and non-focussed meshes respectively. The results are not mesh sensitive which suggest that in all cases the mesh, with quadratic elements, is sufficiently fine. These results can be compared to the data for the J-integral in specimens with clamped ends published in [38]: For the total applied force on the specimen measured as 8595 N, the J-integral value is 6686 J/m^2, which corresponds to an error of 1.47%.

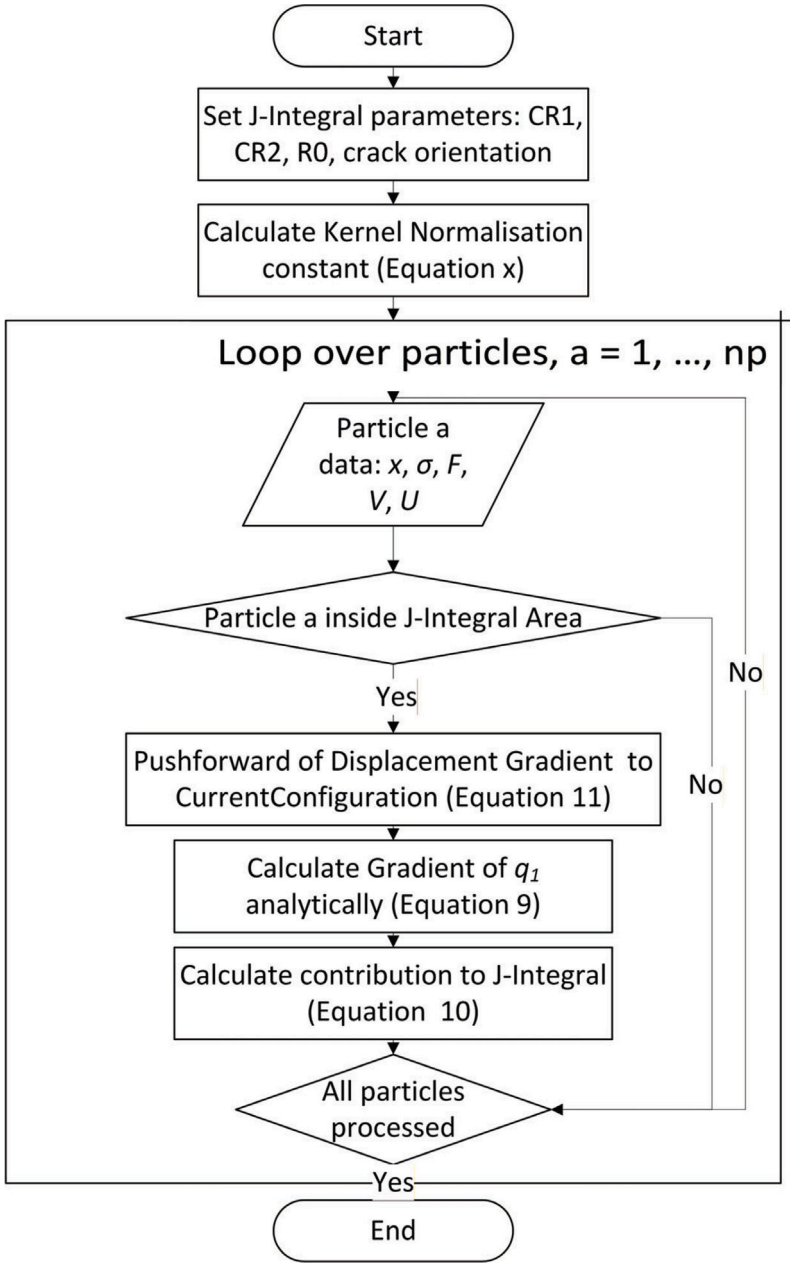

Fig. 3. Block Diagram of the new algorithm to calculate the J-integral in SPH.

5. SPH models

In order to obtain the static stress state in the SENT specimen using the dynamic SPH solver, the specimen was loaded by progressively increasing the displacement and using dynamic relaxation with a dynamic relaxation factor of 0.995. Convergence was assumed when the kinetic energy KE in the system was reduced by four orders of magnitude from the peak value ie. $KE = 0.0001KE_{max}$. The displacement boundary condition is applied through adding layers of particles to each end, with the displacement of these particles prescribed to enforce the boundary condition. An isotropic linear hypoelastic material model was used. The crack was represented by modifying the neighbourhood of particles in the region of the crack. The models were constructed to place the crack tip at the origin, $[0.0\ \text{cm}, 0.0\ \text{cm}]$, of the coordinate system, with the crack aligned with the Y-axis and the crack mouth at position $[0.0\ \text{cm}, -5.0\ \text{cm}]$. The coordinate axes used in the SPH model are shown in Fig. 9. In the region of the crack the rules used to define particle neighbourhoods are that particles that lie within the particles kernel support but are obscured by the crack are excluded from the kernel sums for that particle. With this approach the crack can be considered to be centred between

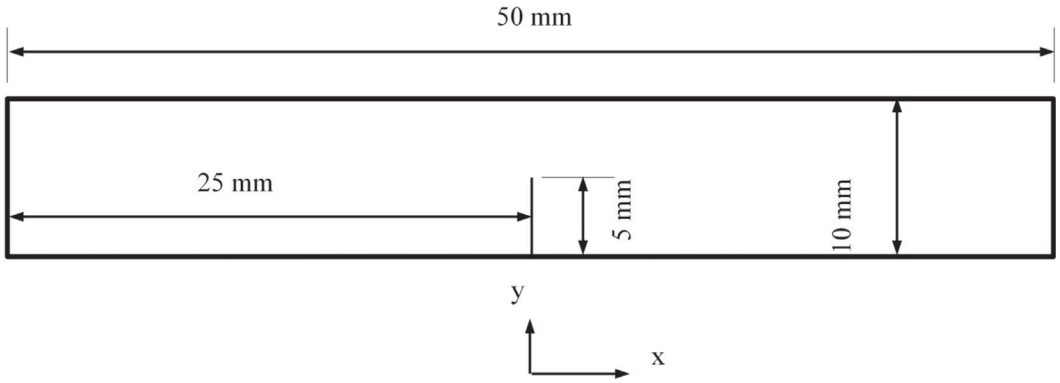

Fig. 4. Geometry of the SENT specimen used.

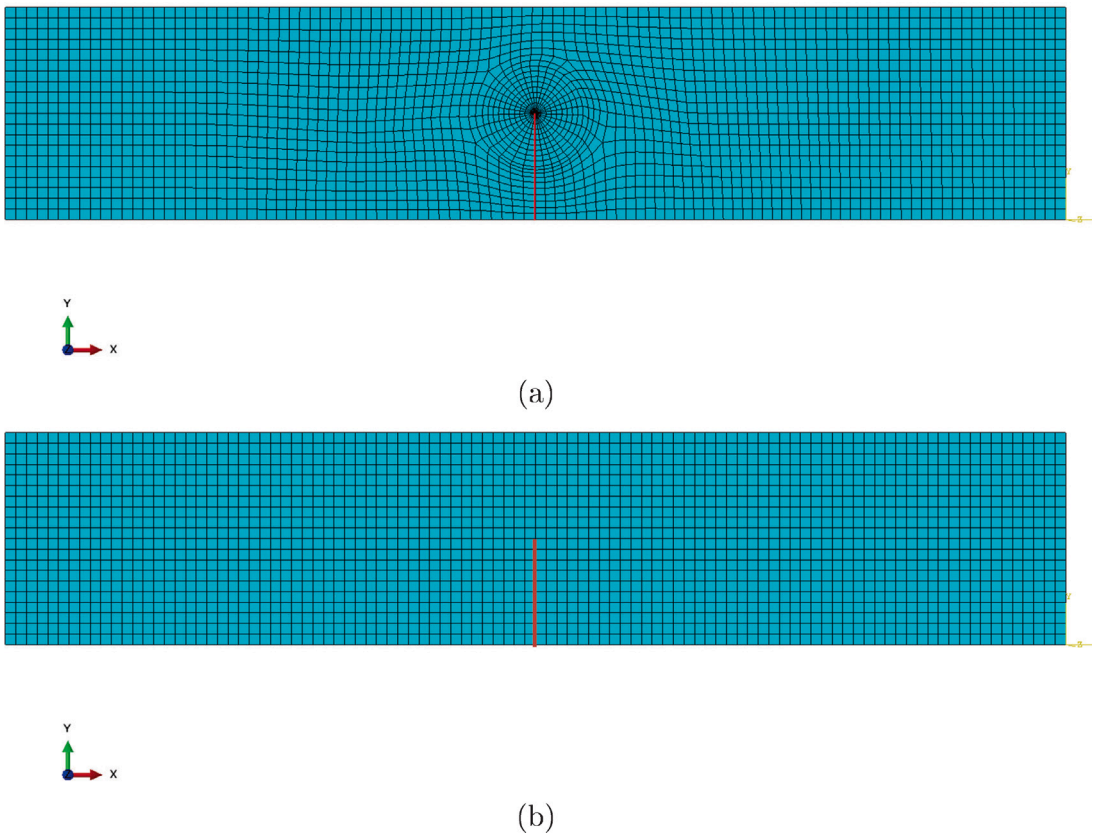

Fig. 5. FEM models with crack shown as red line (a) focused mesh around the crack tip and (b) without the focused mesh.

particles, see Fig. 8. This approach has the advantage that there is no explicit representation of the crack required and no particle properties or behaviours need to be adapted. Models were generated for the same four resolutions used in the not focused mesh FEM models, with the equivalent SPH model having one particle for each element and located at the respective element's centroid. Details of all these models are shown in Table 2, with the particle distributions for the second lowest resolution models shown in Fig. 9.

5.1. SPH model verification of model without crack

To verify the use of dynamic relaxation and the definition of the boundary conditions the SPH80 model (80 × 400 particles) was run without a crack present. This leads to a uniform stress away from the imposed displacement boundary conditions and the

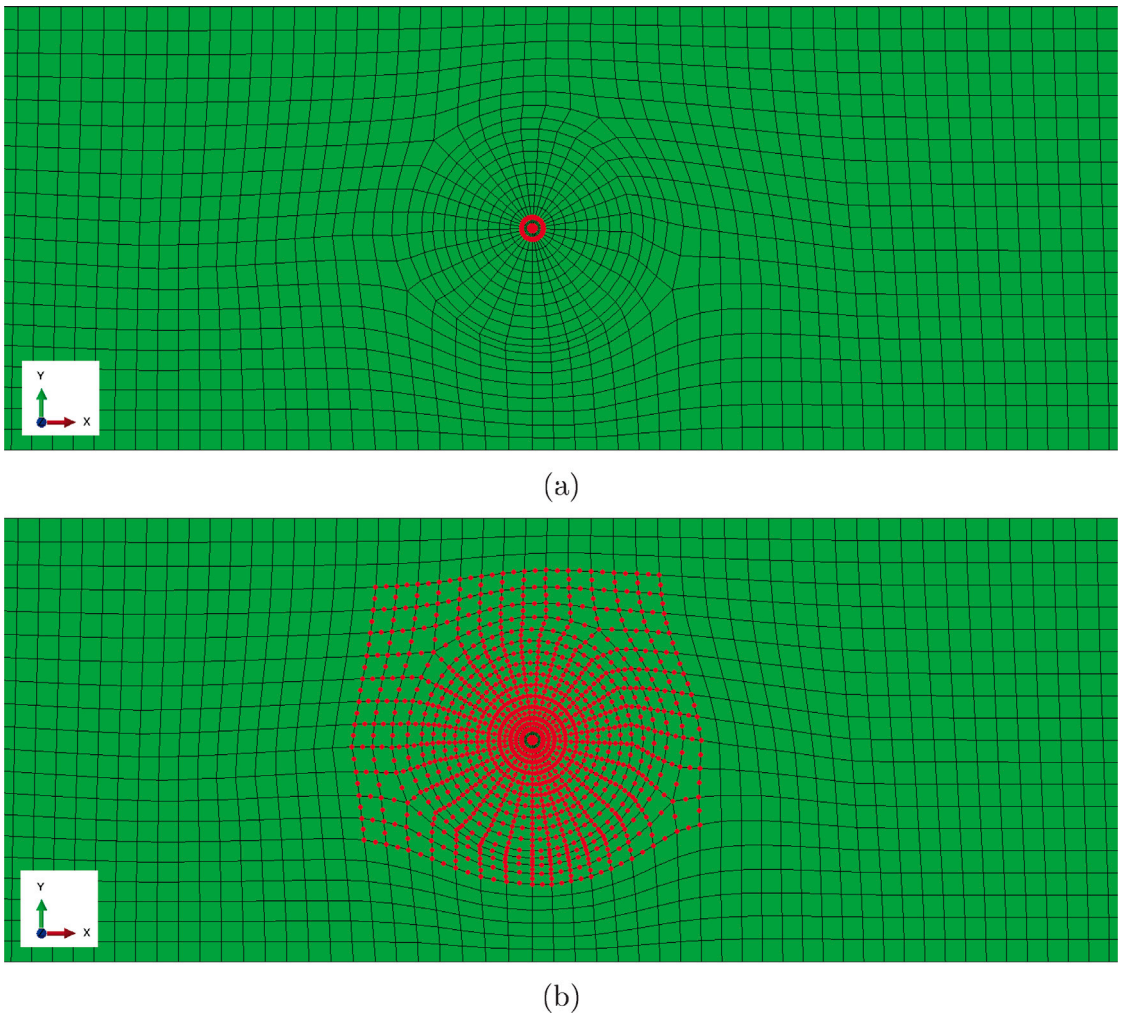

Fig. 6. Node sets for evaluation of J-integral in the Focused 20 model with a focused mesh around the crack tip: (a) nodes forming the second contour; (b) node set forming the 15th (last) contour for this model.

Table 2
Details of SPH models used in this study.

SPH Model	# particles across width	# particles across load direction	Particle spacing in mm
SPH20	20	100	0.5000
SPH40	40	200	0.2500
SPH80	80	400	0.1250
SPH160	160	800	0.0625

analytical plane strain solution is:

$$\sigma = \begin{bmatrix} 234.31 & 0 & 0 \\ 0 & 0 & 0 \\ 0 & 0 & 70.29 \end{bmatrix} \text{MPa} \tag{11}$$

The stress extracted at the central particle in the SPH model is:

$$\sigma = \begin{bmatrix} 235.05 & 0 & 0 \\ 0 & 0 & 0 \\ 0 & 0 & 70.49 \end{bmatrix} \text{MPa} \tag{12}$$

This shows good agreement with the analytical solution with an over-estimate of the direct stress of 0.32%.

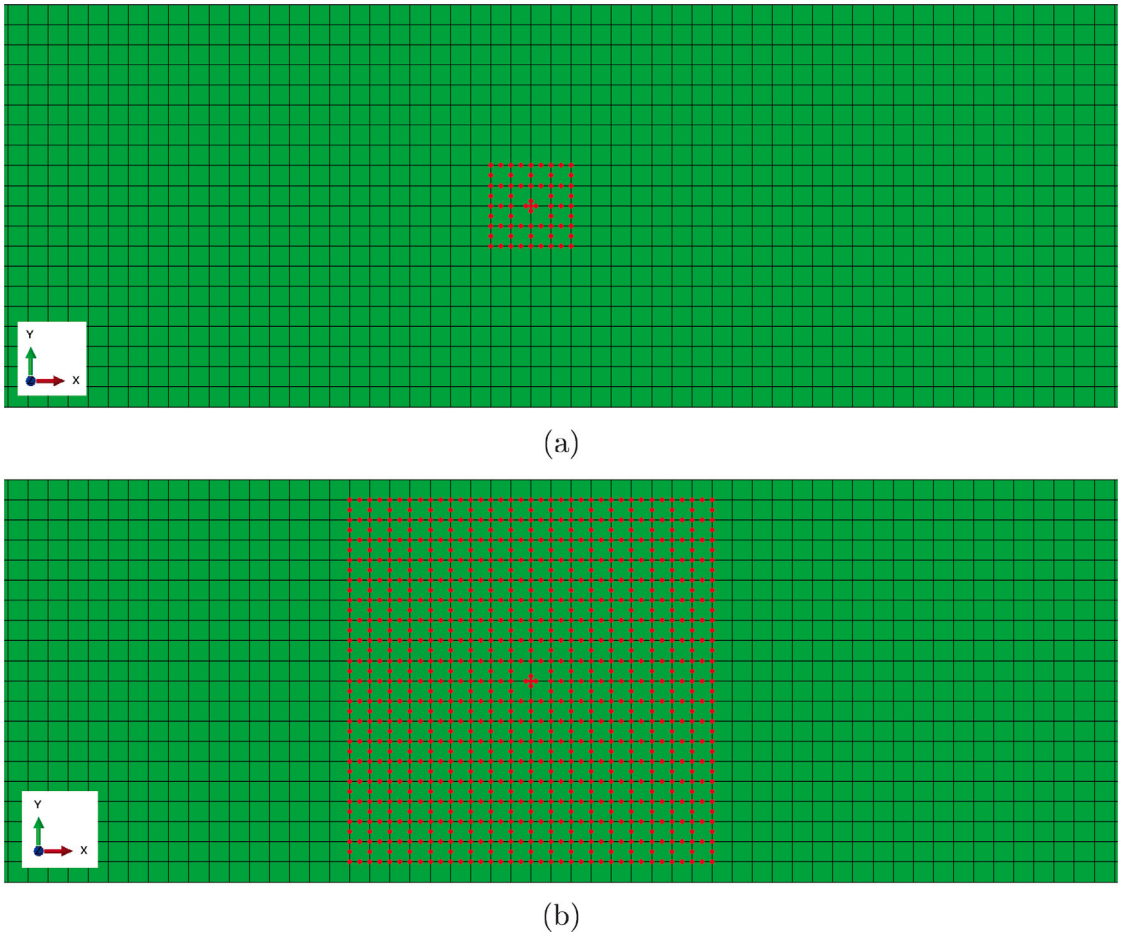

Fig. 7. Node sets for evaluation of J integral in the Not Focused 20 model mesh around the crack tip: (a) nodes forming the second contour; (b) node set forming the 10th (last) contour for this model.

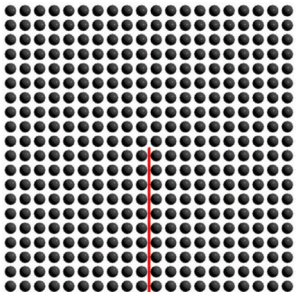

Fig. 8. Detail of particle distribution at crack tip, crack location marked by red line. Crack centred between particles.

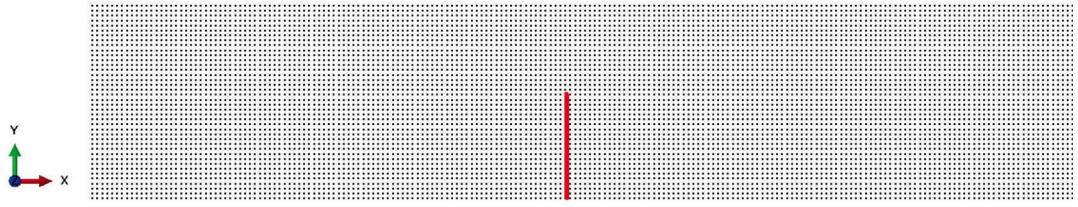

Fig. 9. Particle distribution for model with 40 particles across the specimen width (SPH40). Crack centred between particles and is shown with the red line.

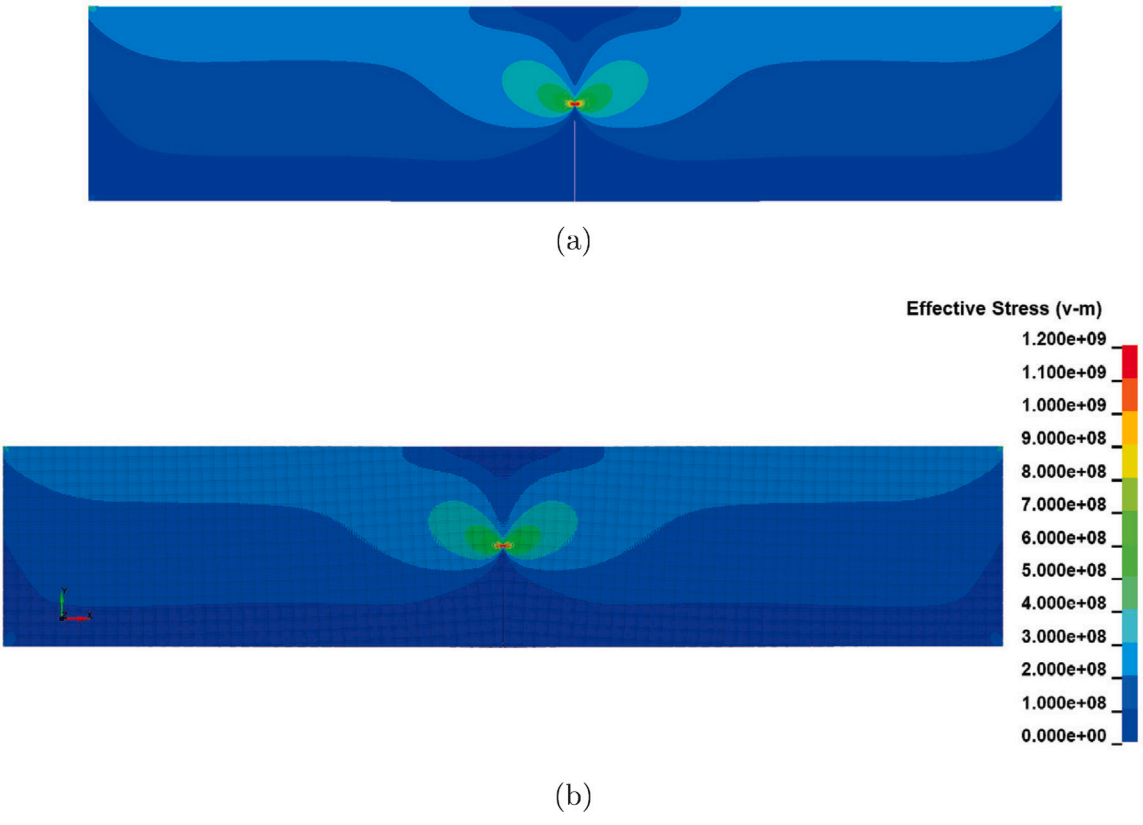

Fig. 10. Comparison of Von Mises stress contours for FE and SPH solutions. Stress units MPa, colour scales and limits are the same for all plots. (a) Reference FE solution FEM160 (b) SPH model, 160 particle model (SPH160).

Table 3
Comparison of Crack Mouth Opening for 160 element/particle FEM and SPH models.

SPH model	Crack Mouth Opening Displacement (CMOD) in mm
SPH160	0.04248
FEM F160	0.04252
FEM NF160	0.04253

5.2. SPH model stress and displacement results

For the comparison of the SPH J -integral calculation algorithm described above to FEM based results it is essential that the calculations are based on equivalent stress and displacement fields. Therefore, in this section a comparison of the stress and displacement results between the SPH and FEM solutions for the SENT specimen (model including a crack) are presented. Fig. 10 shows von Mises stress, Fig. 11 shows axial stress, and the axial displacement field is shown in Fig. 12. Further comparison can be made by considering the stress state around the crack. It can be seen in Fig. 13 that the stress in front of the crack tip closely correlates with the FEM stress field. The opening of the crack at the crack mouth also correlates very well, with difference of 0.12%, as can be seen in Table 3. It is clear from the results in this section that the stress and displacement fields obtained by the SPH method are almost identical to the FEM results, and that these results form an appropriate starting point for the validation of the proposed SPH J-integral calculation algorithm. These results will be presented and discussed in the next section.

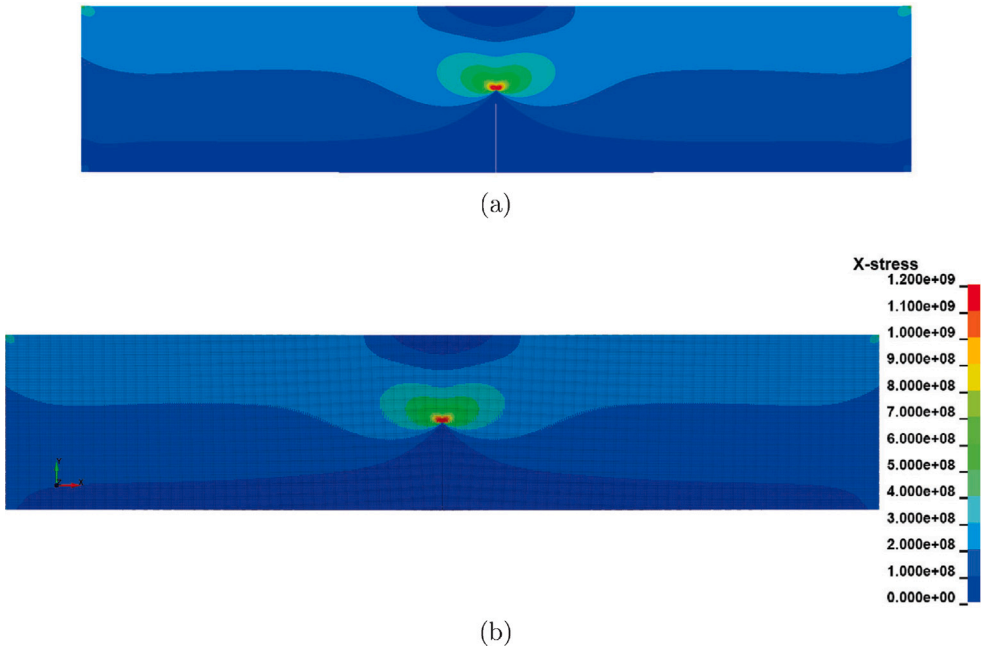

Fig. 11. Comparison of contours of stress component in loading direction for FE and SPH solutions. Stress units MPa, colour scales and limits are the same for all plots. (a) Reference FE solution (FEM160, XX-component) (b) SPH model, 160 particle model (SPH160, XX-component).

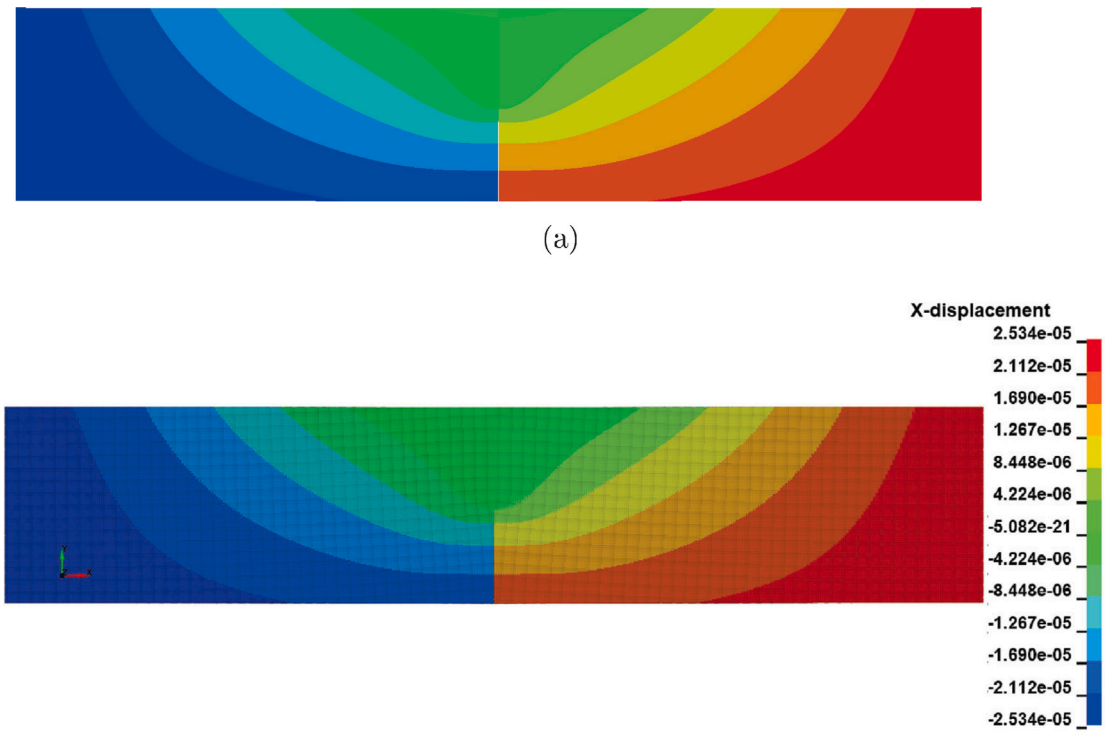

Fig. 12. Comparison of contours of displacement in loading direction for FE and SPH solutions. Displacement units mm, colour scales and limits are the same for all plots. (a) Reference focussed mesh FEM model, 160 element model (b) SPH model, 160 particle model.

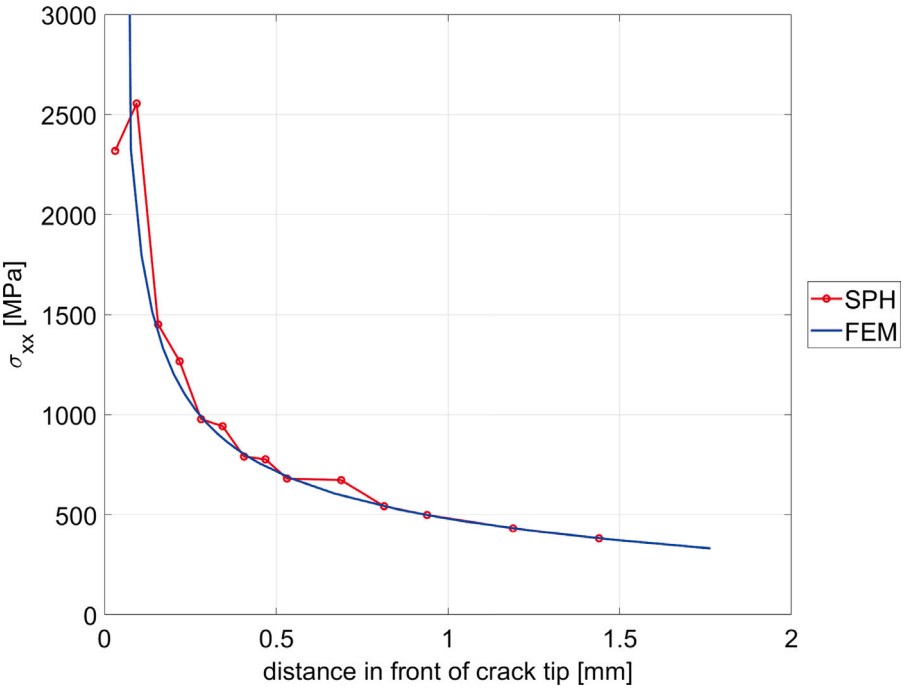

Fig. 13. Direct stress in front of the crack tip for the 160 element/particle models.

6. SPH J-Integral algorithm results and comparison to FEM results

In this section all J-integral results obtained are summarised: four models with different particle spacings or element sizes were used: 20, 40, 80 and 160 particles/elements across the sample width (in the crack direction). Furthermore, the J-integral has been calculated for several contour sizes (i.e. surface integral area), increasing as a function of the inter-particle spacing. The maximum contour used for each discretisation is plot as a red circle in Fig. 14. All images show the full height of SENT sample. For the coarser discretisations, on the left in Fig. 14, the radii that were used were larger since the particle spacing is larger in this case. The actual radius sizes used for each model, and the J-integral values obtained, are listed in Table 4 for the SPH models and Table 5 for FEM. All J-integral values presented in Table 4 are plot in Fig. 15 as a function of contour radius. The experimentally measured value for the J-integral reported in a previous section is represented as a straight line. It can be seen that as expected all models show converging behaviour as the contour radius increases. For the first few contours, with the smaller radii, the values are as expected not converged, and this is the case in both FEM and SPH results. The differences are more pronounced for the SPH results. The FEM results also show some mesh sensitivity, but since the models use quadratic elements stress gradients will be more accurately captured near the crack tip singularity compared to the SPH method which by nature produces smoothed fields and is inherently non-local [40]. The difference between the J-integral values for the focused and non-focused mesh results is very small, 6785 J/m^2 versus 6786 J/m^2 (a difference of 0.015%).

If we consider the results for the models with the most refined discretisation (160 particles/elements) then it can be seen that the SPH results converge to almost the same value as the FEM result with a non-focussed mesh: 6862 J/m^2 vs. 6785 J/m^2, a difference of 1.13%. When comparing to the FEM results with the focussed mesh the converged values are 6862 J/m^2 and 6786 J/m^2, a difference of 1.12%. This demonstrates that the algorithm proposed to calculate the J-integral in SPH works as well as FEM based J-integral calculations.

7. Accuracy of SPH J-Integral calculation

Analysing the results in Fig. 15 in more detail it can be seen that the coarser models (SPH20 and SPH40) do not fully converge even for the largest contours. This may be due to the magnitude of these contours is limited by the size of the specimen (see also Fig. 14a and b). Nevertheless, the final values of 6900 J/m^2 and 6929 J/m^2 obtained are still close to the 6786 J/m^2 (1.7 and 2.1% difference) of the FEM model with 160 elements. For the more refined models, SPH80 and SPH160, the results show clear

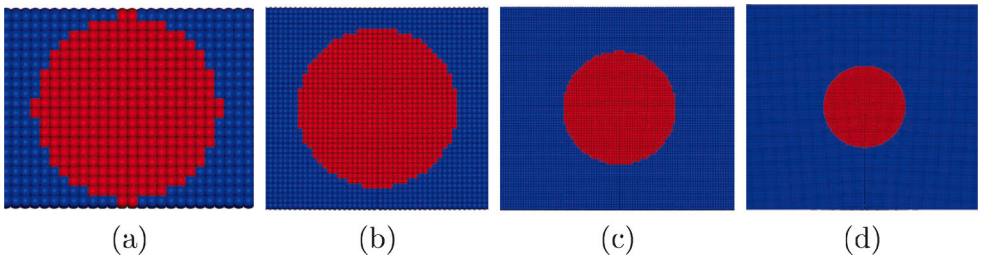

Fig. 14. Largest J-integral area, highlighted in red, used for (a) SPH20, (b) SPH40, (c) SPH80 and (d) SPH160 models.

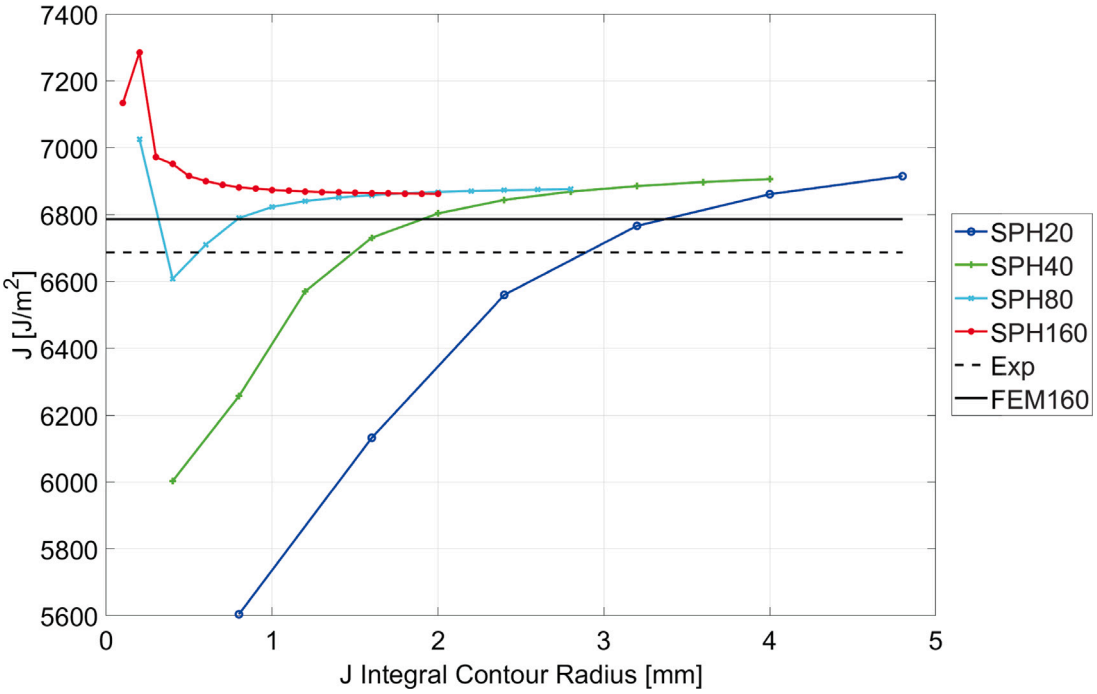

Fig. 15. Plot of J-integral value against J-Integral domain radius. The value of J-integral from the reference FE solutions and experimental results are marked as horizontal lines.

convergence with differences of 1.7% and 1.1% respectively. To understand the convergence behaviour better it is useful to plot the J-integral value as a function of number of particles in the J-integral sum, see Fig. 16a, and the J-integral value as a function of some measurement of the contour size, in Fig. 16b the ratio of the contour radius to the particle spacing. From these plots it can be seen that if the J-integral is calculated using around 200 particles then the calculation has mostly converged and if more than 500 particles are used the value differs only 0.23% from the final value (6881 J/m^2 vs. 6862 J/m^2 for the SPH160 model). Instead of number of particles another guideline for the selection of the J-integral contour can be the ratio of the contour ratio to the particle spacing shown in Fig. 16b. This ratio can be seen as the equivalent to the contour number (successive rings of elements around the crack tip) in FEM. If this measure is used a value of 10 appears adequate. This is larger than the 3 layers that the FEM results need for convergence, but the FEM model uses quadratic elements which improves convergence, especially for the stress field.

8. Effect of choice of q_1 function on results

Until now the q_1 weighting function in the calculation of the J-integral has been the cubic B-spline kernel function. In other words, q_1 was chosen to be the same shape (albeit scaled differently) as the kernel function used to perform SPH gradient and divergence calculations. Using the cubic B-spline in a first instance is justified since after rescaling it satisfies all the conditions for the q_1 function (equal to 1 at the centre and zero on the boundary and sufficiently smooth), as well having been demonstrated to work well as a weighting function (kernel) in SPH integrals. Although the results presented above show that the cubic B-spline is an adequate choice of q_1 function, in this section it will be investigated how other functions perform. For this, the Wendland C2 kernel,

Table 4
Values of J-Integral for SPH models ("–" = no value for this size).

Domain radius (mm)	SPH20	SPH40	SPH80	SPH160
0.1	–	–	–	7133
0.2	–	–	6113	7285
0.3	–	–	–	6971
0.4	–	4801	6366	6950
0.5	–	–	–	6914
0.6	–	–	6589	6900
0.7	–	–	–	6889
0.8	4325	5787	6734	6881
0.9	–	–	–	6877
1.0	–	–	6797	6874
1.1	–	–	–	6871
1.2	–	6339	6833	6873
1.3	–	–	–	6869
1.4	–	–	6855	6867
1.5	–	–	–	6865
1.6	5573	6613	6869	6864
1.7	–	–	–	6863
1.8	–	–	6880	6863
1.9	–	–	–	6862
2.0	–	6741	6888	6862
2.2	–	–	6893	–
2.4	6299	6815	6898	–
2.6	–	–	6901	–
2.8	–	6861	6904	–
3.2	6643	6891	–	–
3.6	–	6913	–	–
4.0	6806	6929	–	–
4.8	6900	–	–	–

Table 5
Values of J-Integral for Focussed mesh (F) and Non-Focussed mesh (NF) FEA models ("|" = same value as above, "–" = no value for this size).

Domain radius (mm)	FEM20		FEM40		FEM80		FEM160	
	F	NF	F	NF	F	NF	F	NF
0.0625	–	–	–	–	–	–	6794	6789
0.1250	–	–	–	–	6793	6789	6787	6783
0.1875	–	–	–	–	–	–	6786	6786
0.2500	–	–	6792	6789	6786	6783	6785	|
0.3125	–	–	–	–	–	–	|	|
0.3750	–	–	–	–	6786	6786	|	|
0.4375	–	–	–	–	|	|	|	|
0.5000	6789	6789	6784	6783	|	|	|	|
0.6250	–	–	–	–	|	|	|	|
0.7500	–	–	6783	6786	|	|	|	|
0.8750	–	–	|	|	|	|	|	|
1.0000	6781	6783	|	|	|	|	|	|
1.250	–	–	|	|	|	|	|	|
1.500	6780	6786	|	|	|	|	|	|
1.750	|	|	|	|	|	|	|	|
2.000	|	|	|	|	|	|	|	|
2.250	|	|	|	|	|	|	|	|
2.500	|	|	6783	6786	6786	6786	6785	6786
3.000	|	|	–	–	–	–	–	–
3.500	|	|	–	–	–	–	–	–
4.000	6780	6786	–	–	–	–	–	–

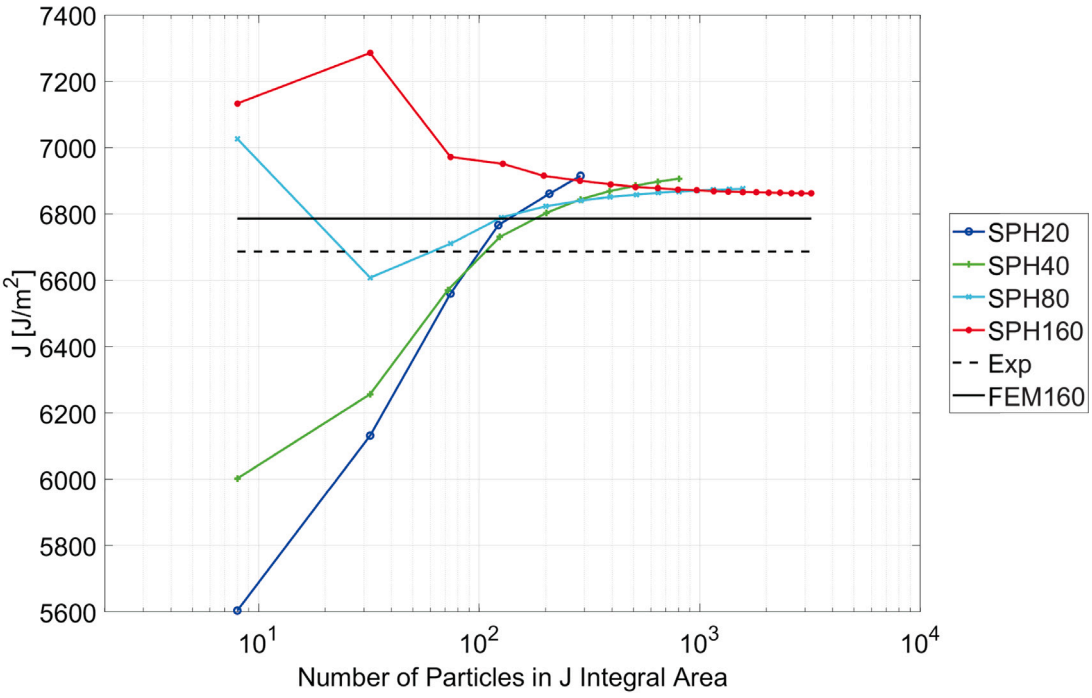

(a)

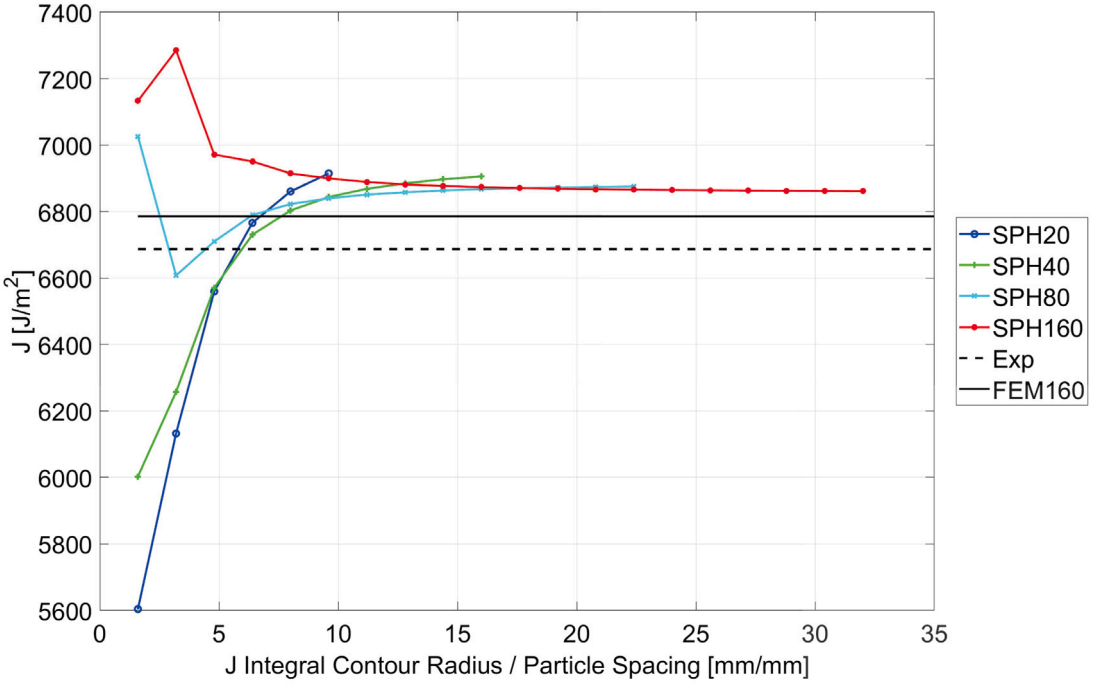

(b)

Fig. 16. Plot of (a) J-integral against number of particles in the J-integral contour and (b) J-integral against ratio of contour radius to particle spacing. The value of J-integral from the reference FE solutions and experimental results are marked as horizontal lines.

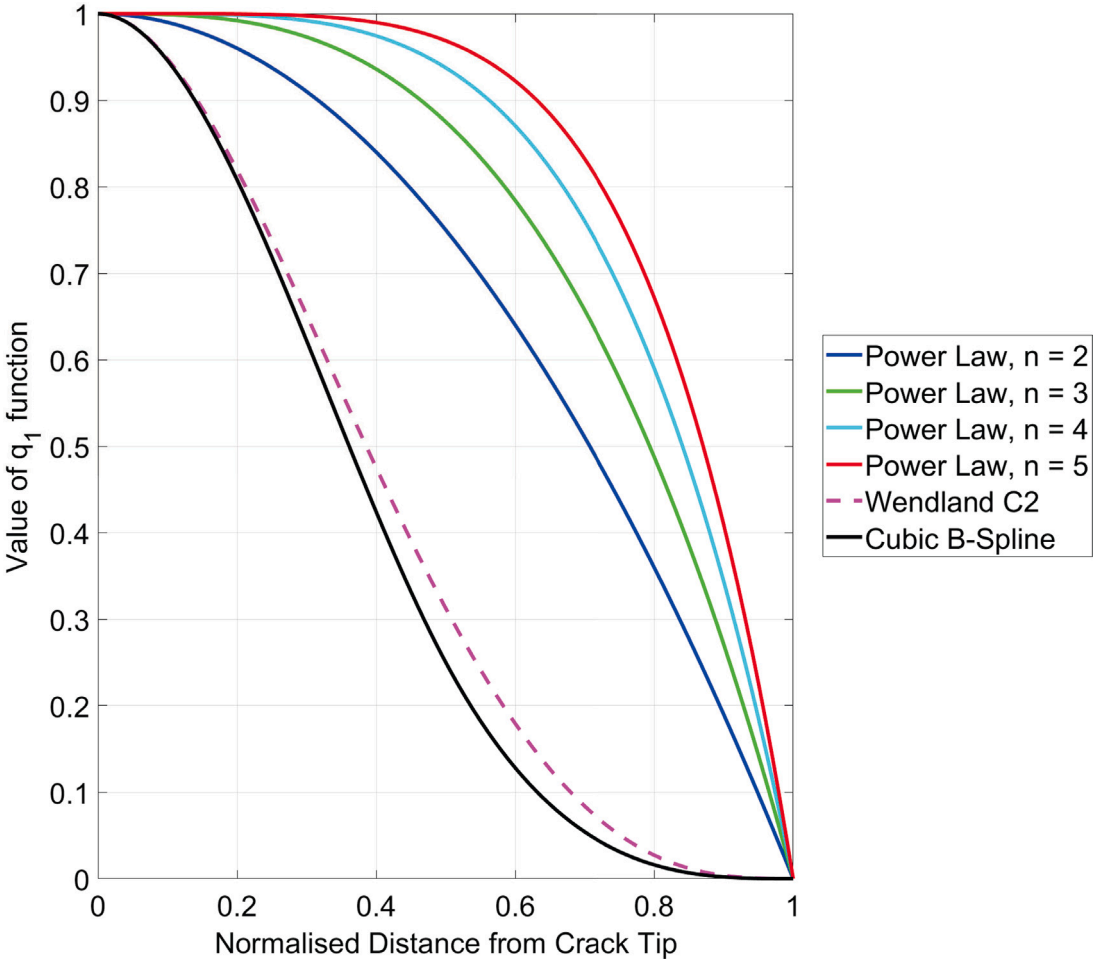

Fig. 17. Plot of different q_1 functions used.

another common SPH kernel function, and a power law function will be tested. The Wendland kernel has the following form:

$$q_1 = (1-z)^3\,(1+3z) \tag{13}$$

The power law function that was chosen is:

$$q_1 = 1 - z^n \tag{14}$$

where $z = \left|\mathbf{x}_i - \mathbf{x}_j\right| / R_{c_2}$, with R_{c_2} the outer radius of the J-integral domain. The choice of this power law function was motivated by the fact for higher values of the power n the function will look similar to the q_1 function used in FEM (i.e. 1 inside most of the domain and tending towards zero near the outer boundary) but retaining smooth derivatives like the SPH kernel functions. The functions used are plot in Fig. 17. The results obtained with the Wendland C2 kernel and the power law function with $n \in (2,3,4,5)$ are plot in Fig. 19. It can be seen that the use of the Wendland C2 kernel q_1 function yields a J-integral value that is slightly closer to the reference FEM solution. The convergence rate is similar to the cubic B-spline kernel q_1 function. For the power law results the results show a different type of behaviour. Irrespective of the value of the power n it is clear that while the J-integral values tend towards the same result, a large amount of oscillation is present in the results. The level of oscillation increases with the power n. Looking at 18 it can be observed that the spatial derivative of q_1, dq_1/dx, which appears in the J-integral, will be biased more and more towards the outer edge of the integral area, and the largest values of dq_1/dx will be immediately next to the outer boundary. This means that the contribution of the particles nearer the outer radius will become more important. Hence with this type of function the value of the J-integral will be very sensitive to the specific distribution of particles near the outer edge and this can explain the oscillation observed. In contrast, both SPH interpolation kernel based functions have much more gradual change of gradient across the area, see Fig. 18. This means that the contribution of each particle to the J-integral is much more even. Furthermore,

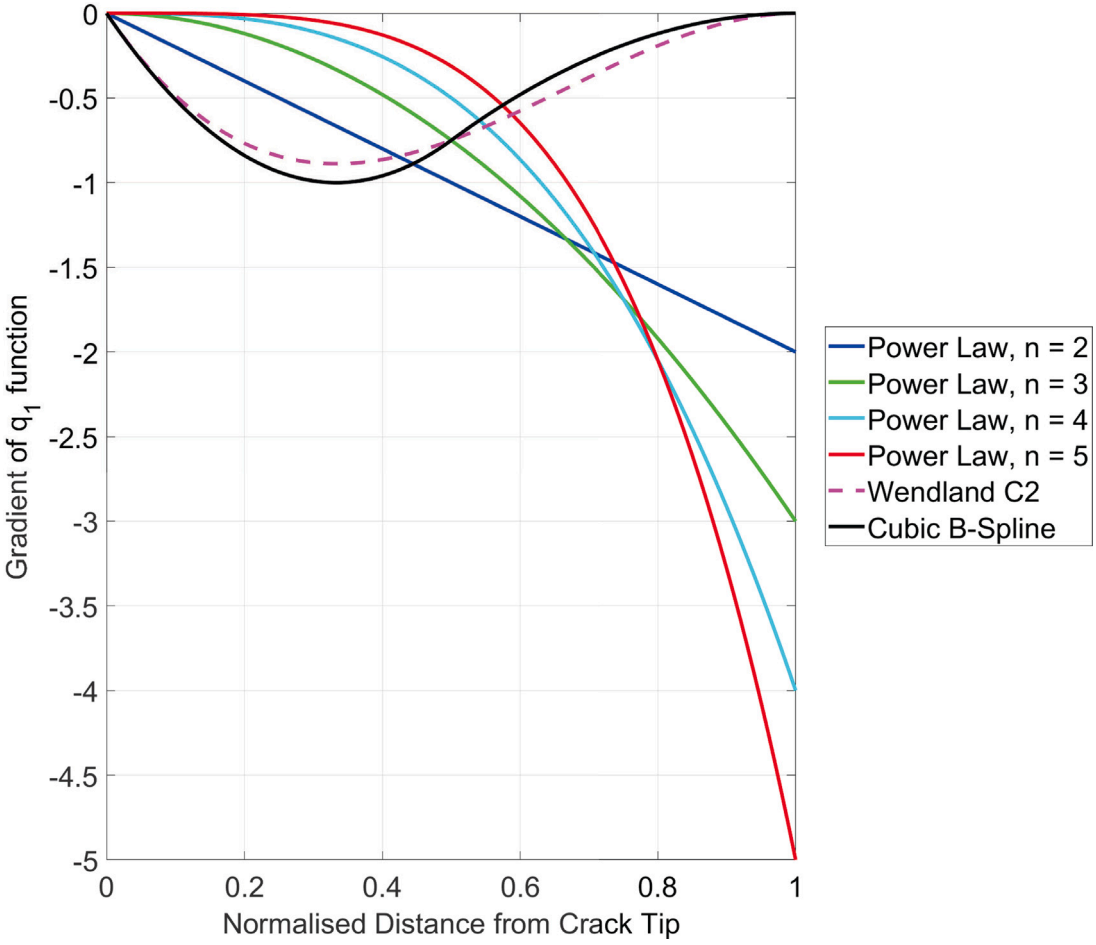

Fig. 18. Plot of derivative different q_1 functions used.

the derivative of the Wendland C2 kernel changes slightly more gradual than the cubic B-spline which could explain the better convergence of the Wendland C2 kernel versus the cubic B-spline. Overall, these results indicate that with this J-integral calculation algorithm using a q_1 function that has a gradual change of gradient over the domain is a key factor in obtaining accurate results and good convergence.

9. Application: Single Edge Notch Bend (SEND)

In order to evaluate the sensitivity of the results to the stress state in the sample the same specimen was used but this time in a Single Edge Notch Bend (SEND) configuration. This model is a 3-point bend test configuration, as shown in Fig. 20. Specimen geometry and material properties are the same as previously, but this time the specimen is supported on two 4 mm diameter rollers with centres 40 mm apart. The crack is located at mid-way between these rollers. Directly above the crack, the third roller, also with 4 mm diameter, is given a 1 mm vertical displacement to load the sample. The rollers are modelled as a rigid material. As in the previous SPH models the Total-Lagrangian kernel formulation has been used. The interaction between the sample and the rollers is handled through a frictionless particle-to-particle contact algorithm, details of which can be found in [41]. Based on the results of the previous sections the J-integral is calculated using a Wendland C2 shaped q_1 function, as this provided the best convergence. Only the two most refined SPH models (SPH80 and SPH160) were run in this case. Similar to the SENT case, a reference FEM model of this test was also developed. The sample has the same mesh and material properties as the FEM160 SENT case. The rollers are modelled as a rigid material, and contact is handled through a frictionless contact algorithm. The xx-stress field is plot for both FEM and SPH models in Fig. 21. It can be seen that the stress field obtained by both models is very similar. Crucially the J-integral values obtained are also in good agreement, see Fig. 22: the FEM model predicts a J-integral value of $749 \cdot 10^3$ J/m^2, while the SPH models converges to values of $732 \cdot 10^3$ J/m^2 for the SPH80 and $744 \cdot 10^3$ J/m^2 for the SPH160 model, a difference of 2.3% and 0.8%

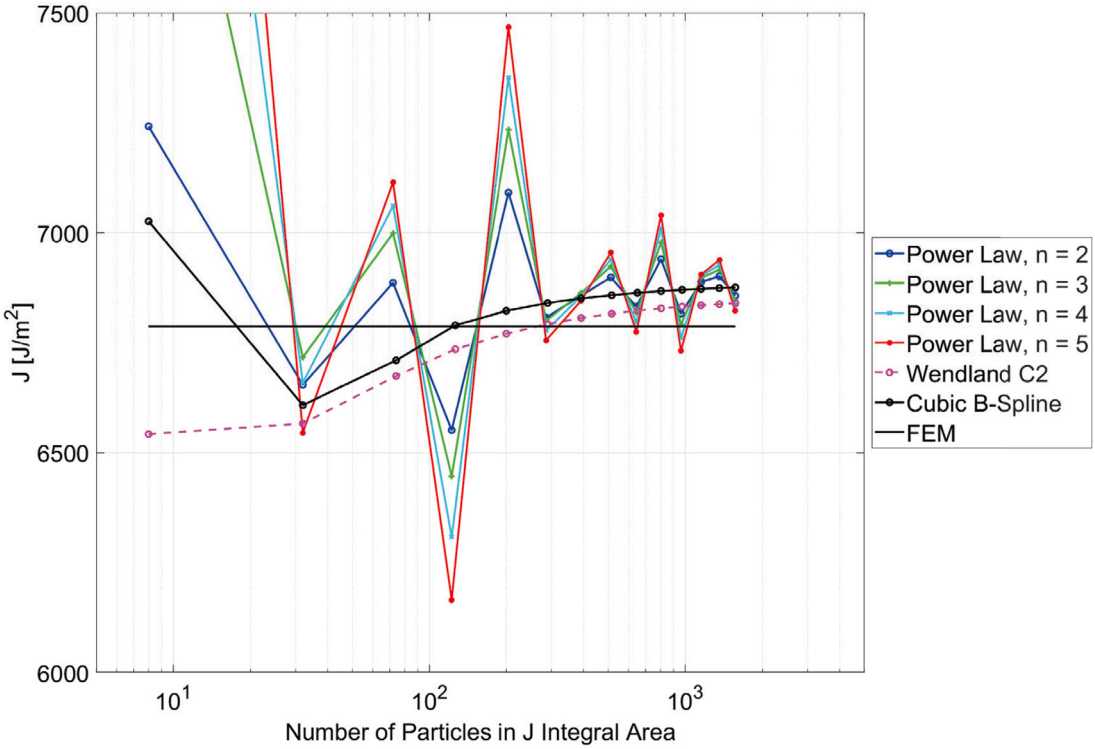

Fig. 19. Plot of J-integral against number of particles for different choices of q_1 function.

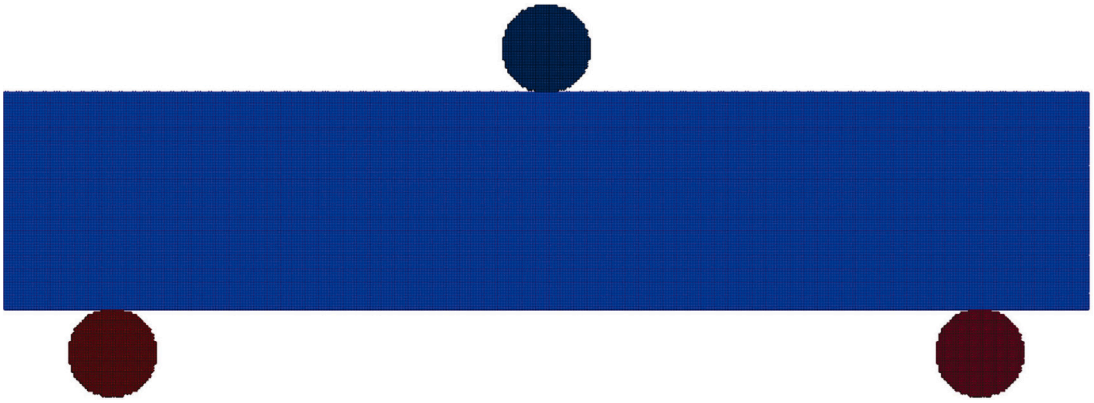

Fig. 20. Initial configuration of SENB test.

respectively. With 500 particles in the support, the difference to the FEM solution is 3.3% and 2.4% respectively. So This good agreement indicates the robustness of the proposed algorithm for different configurations.

10. Conclusion

In this paper the calculation of the J-Integral in SPH was investigated. A new algorithm for the calculation of the J-Integral was proposed and it was demonstrated that the J-Integral calculated using this algorithm had a 1.0 to 3.0% difference compared to a refined FEM model with quadratic elements. It was demonstrated that compared to the algorithms used in FEM, the definition

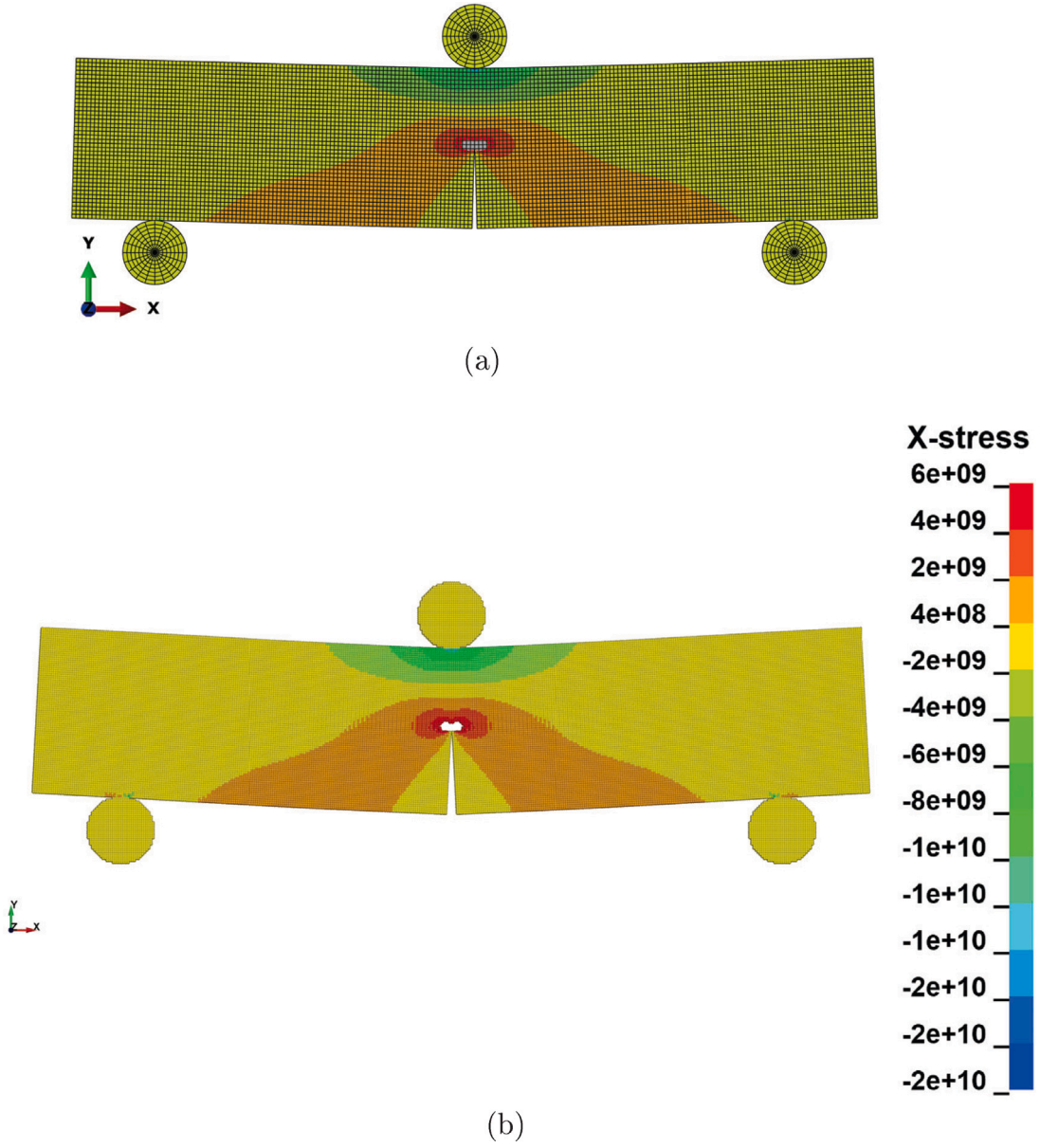

Fig. 21. Plot of deformed shape and XX-stress component for (a) FEM model and (b) SPH model.

of the J-Integral in SPH can be significantly simplified by using a novel approach in choosing an SPH kernel type function for the weighting function q_1. Based on the functions studied it can be concluded that a function with a gradually changing gradient from crack tip to outer radius, such as the functions typically used as SPH kernels, provide good results. Other functions, such as the power law studied in this paper can produce poor convergence in the form of large oscillations in the calculated value of the J-integral with increasing area. Compared to algorithms currently used in FEM, the proposed algorithm is radically different in that the J-integral is obtained by evaluating the gradient of the q_1 function analytically rather than through interpolation functions, resulting in a significant simplification of the algorithm compared to FEM. This aspect also demonstrates the potential benefits of SPH for fracture mechanics. In terms of ensuring accuracy of the results using this algorithm: an analysis of the results for SENT and SENB configurations with different particle spacings and contour radii showed that as a guideline around 500 particles in J-Integral is required to obtain results that are within 2.5% of a similar FEM model. An alternative measure is to choose an adequate J-integral radius that is minimum 10 times the particle spacing. The extension of the algorithm to 3D needs to be addressed in future research.

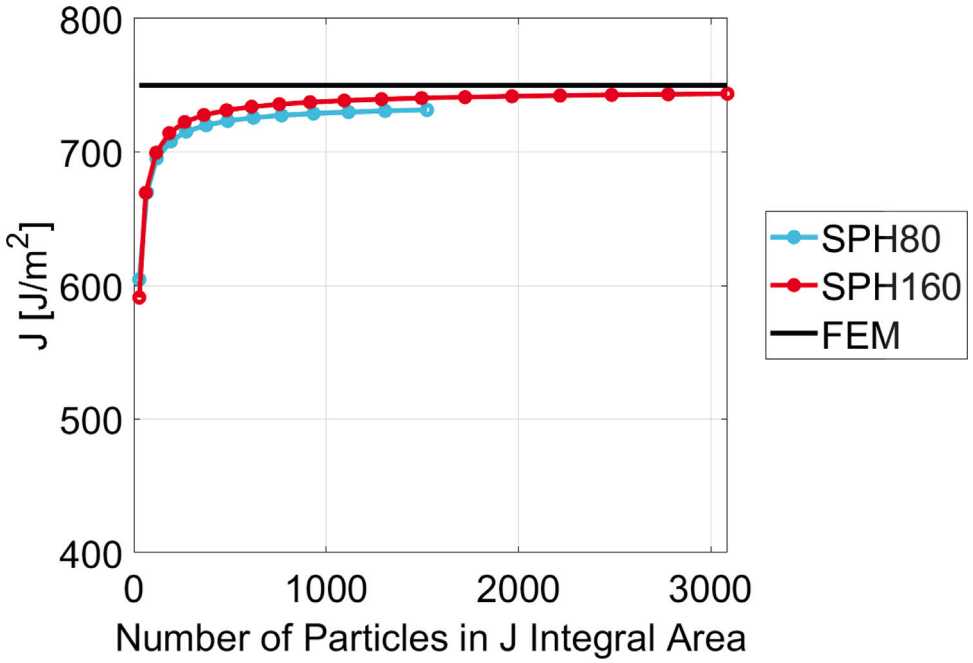

Fig. 22. Plot of J-integral against number of particles for SENB configuration.

Furthermore, the accuracy of the point-wise integration of the J-integral with an analytical evaluation of the q_1 weighting function proposed here could also be assessed for FEM based results.

CRediT authorship contribution statement

Tom De Vuyst: Writing – review & editing, Writing – original draft, Visualization, Validation, Software, Methodology, Investigation, Formal analysis, Conceptualization. **Rade Vignjevic:** Writing – review & editing, Writing – original draft, Methodology, Investigation, Formal analysis, Conceptualization. **Nenad Djordjevic:** Writing – review & editing, Writing – original draft, Visualization, Validation, Investigation, Formal analysis, Data curation. **Marius Gintalas:** Writing – review & editing, Writing – original draft, Validation, Investigation, Formal analysis, Data curation. **Kevin Hughes:** Writing – review & editing, Writing – original draft, Validation, Methodology.

Declaration of competing interest

The authors declare that they have no known competing financial interests or personal relationships that could have appeared to influence the work reported in this paper.

Data availability

The data that has been used is confidential.

References

[1] Lucy LB. A numerical approach to the testing of the fission hypothesis. Astron J 1977;82:1013–24.
[2] Gingold RA, Monaghan JJ. Smoothed particle hydrodynamics: theory and application to non-spherical stars. Mon Not R Astron Soc 1977;181(3):375–89.
[3] Libersky LD, Petschek AG. Smooth particle hydrodynamics with strength of materials. In: Trease HE, Fritts MF, Crowley WP, editors. Advances in the free-Lagrange method including contributions on adaptive gridding and the smooth particle hydrodynamics method. Lecture notes in physics, vol. 395, Berlin, Heidelberg: Springer; 1991, p. 248–57.
[4] Randles PW, Libersky LD. Smoothed particle hydrodynamics: some recent improvements and applications. Comput Methods Appl Mech Engrg 1996;139(1–4):375–408.
[5] Vignjevic R, Campbell J. In: Hiermaier S, editor. Review of development of the smooth particle hydrodynamics (SPH) method in predictive modelling of dynamic processes. Springer; 2009.
[6] Hutchinson JW, Mear M, Rice JR. Crack paralleling an interface between dissimilar materials. ASME J Appl Mech 1987;54:828–32.
[7] Matos PPL, McMeeking RM, Charalambides PG, Drory MD. Int. J. Fract. 1989;40:235–54.
[8] Rice JR. A path independent integral and the approximate analysis of strain concentration by notches and cracks. J Appl Mech 1968;35:379–86.

[9] Hutchinson JW. Plastic stress and strain fields at a crack tip. J Mech Phys Solids 1968;16(5):337–42.
[10] Hauck B, Szekrényes A. Advanced finite element analyses to compute the J-integral for delaminated composite plates. Appl Math Model 2024;126:584–605.
[11] Zheng W, Kassapoglou C. Energy method for the calculation of the energy release rate of delamination in composite beams. J Compos Mater 2019;53(4):425–43.
[12] British Standards Institution. BS 7910:2019 guide to methods for assessing the acceptability of flaws in metallic structures. London, UK: BSI Standards Publication; 2019.
[13] Dassault Systèmes. Abaqus 2024 documentation. Providence, RI, USA: SIMULIA User Assistance; 2024, Available at: https://www.3ds.com/support/documentation/.
[14] Livermore Software Technology Corporation. LS-DYNA keyword user's manual, Volume I–III, R15. Ansys, Inc; 2025, Available at: https://lsdyna.ansys.com/manuals/.
[15] Shivakumar KN, Tan PW, Newman JC. A virtual crack-closure technique for calculating stress intensity factors for cracked three dimensional bodies. Int J Fract 1988;36:R43–50.
[16] Karmakov S, Cepero-Mejías F, Curiel-Sosa J-L. Numerical analysis of the delamination in CFRP laminates: VCCT and XFEM assessment. Compos Part C 2020;2:100014.
[17] Belytschko T, Black T. Elastic crack growth in finite elements with minimal remeshing. Int J Numer Methods Eng 1999;45(5):601–20.
[18] Moes N, Dolbow J, Belytschko T. A finite element method for crack growth without remeshing. Internat J Numer Methods Engrg 1999;46(1):131–50.
[19] Mohammadpour A, Paluszny A, Zimmerman RW. A robust 3D finite element framework for monolithically coupled thermo-hydro-mechanical analysis of fracture growth with frictional contact in porous media. Comput Methods Appl Mech Engrg 2025;434:117557.
[20] Gintalas M, Ainsworth RA, Scenini F. T-stress solutions for through-wall circumferential cracks in straight pipes under bending. Int J Press Vessels Pip 2017;152:27–37.
[21] Rahimi MN, Moutsanidis G. An SPH-based FSI framework for phase-field modeling of brittle fracture under extreme hydrodynamic events. Eng Comput 2023;39:2365–99.
[22] De Vuyst T, Vignjevic R, Bourne NK, Campbell J. Evaluation of the SPH method for the modelling of spall in anisotropic alloys. In: DCSSS conference. Cambridge; 2002.
[23] De Vuyst T, Vignjevic R. Total Lagrangian SPH modelling of necking and fracture in electromagnetically driven rings. Int J Fract 2013;180:53–70.
[24] Ferraro ES, Seidl M, De Vuyst T. Investigation on fragmentation of pyrophoric alloy samples during taylor test using SPH. EPJ Web Conf 2021;250:02008.
[25] Tazoe K, Tanaka H, Oka M, Yagawa G. Analyses of fatigue crack propagation with smoothed particle hydrodynamics method. Eng Fract Mech 2020;228:106819.
[26] Douillet-Grellier T, Jones BD, Pramanik R, Pan K, Albaiz A, Williams JR. Mixed-mode fracture modeling with smoothed particle hydrodynamics. Comput Geotech 2016;79:73–85.
[27] Wiragunarsa M, Zuhal LR, Dirgantara T, Putra IS. SPH method for crack growth modelling using particle deletion and interaction pair-based framework. Procedia Struct Integr 2024;52:583–93.
[28] Veera Ganesh K, Ibne Islam Md R, Patra PK, Travis KP. A pseudo-spring based SPH framework for studying fatigue crack propagation. Int J Fatigue 2022;162:106986.
[29] Feng R, Fourtakas G, Rogers BD, Lombardi D. A general smoothed particle hydrodynamics (SPH) formulation for coupled liquid flow and solid deformation in porous media. Comput Methods Appl Mech Engrg 2024;419:116581.
[30] Bergkamp EA, Verhoosel CV, Remmers JJC, Smeulders DMJ. A thermodynamically consistent J-integral formulation for fluid-driven fracture propagation in poroelastic continua. J Mech Phys Solids 2023;170:105082.
[31] Song H, Rahman SS. An extended J-integral for evaluating fluid-driven cracks in hydraulic fracturing. J Rock Mech Geotech Eng 2018;10(5):832–43.
[32] Guan X-S, Sun P-N, Zhang X, Lyu H-G, Xu Y. SPH simulations of complex 3D fluid–solid interactions with an improved single-layer particle boundary technique preventing boundary penetration. Ocean Eng 2024;312:119061.
[33] Vignjevic R, Reveles JR, Campbell J. SPH in a total Lagrangian formalism, meshless methods. Comput Methods Eng Sci 2006;14(3):181–98.
[34] Shih CF, Moran B, Nakamura T. Energy release rate along a three-dimensional crack front in a thermally stressed body. Int J Fract 1986;30:79–102.
[35] Nakamura T, Shih CF, Freund LB. Analysis of a dynamically loaded three-point-bend ductile fracture specimen. Brown University Report ONR0365/1, 1985; 1986, In print: Engineering Fracture Mechanics.
[36] Nakamura T, Shih CF, Freund LB. Computational methods based on an energy integral in dynamic fracture. Int J Fract 1985;27:229–43.
[37] Li FZ, Shih CF, Needleman A. A comparison of methods for calculating energy release rate. Eng Fract Mech 1985;21:405–21.
[38] John Reji, Rigling Brian. Effect of height to width ratio on k and CMOD solutions for a single edge cracked geometry with clamped ends. Eng Fract Mech 1998;60(2):147–56.
[39] Lindström P, Jonsson A, Jernberg A, Østby E. Non-linear fracture mechanics in LS-dyna and LS-PrePost. In: 10th European LS-dyna conference. Würzburg, Germany: Dynamore GmbH; 2015.
[40] Vignjevic R, De Vuyst T, Campbell J. The nonlocal, local and mixed forms of the SPH method. Comput Methods Appl Mech Engrg 2021;387.
[41] Vignjevic R, De Vuyst T, Campbell JC. A frictionless contact algorithm for meshless methods. Comput Model Eng Sci 2006;13(1):35–48.